

LETTER

PISE: Physics-Anchored Semantically-Enhanced Deep Computational Ghost Imaging for Robust Low-Bandwidth Machine Perception

Tong WU[†], *Student Member*

SUMMARY We propose PISE, a physics-informed deep ghost imaging framework for low-bandwidth edge perception. By combining adjoint operator initialization with semantic guidance, PISE improves classification accuracy by 2.57% and reduces variance by 9x at 5% sampling.

key words: Computational ghost imaging, Low-bandwidth sensing, Physics-informed deep learning, Edge perception

1. Introduction

Many IoT and robotic systems cannot afford transmitting full-frame images over channels with limited bandwidth [1], strict energy budgets, or intermittent connectivity. This motivates a machine-centric perspective [2]: instead of image formation for humans, we optimize the sensing efficiency for machines, where the goal is not perfect pixel recovery but retaining semantic information from sparse observations.

Computational Ghost Imaging (CGI), also known as single-pixel imaging, offers hardware-efficient compressive acquisition [3]. By modulating the light field using structured spatial patterns and measuring aggregated intensity with a bucket detector, the scene can be optically compressed before readout. Recent advances have enabled open-source toolboxes [4] and efficient fiber-laser-based implementations [5] for practical single-pixel imaging systems. However, at deep undersampling (e.g., 5%), the inverse problem becomes massively underdetermined. Traditional reconstruction methods fail in different ways: physics-based solvers exhibit aliasing artifacts [6]; end-to-end deep networks [7–10] trained with mean squared error (MSE) converge to an overly smoothed conditional mean; and GAN-based methods [11] produce sharp but measurement-inconsistent hallucinations. Deep unfolding approaches [12, 13] have shown promise in balancing interpretability with performance.

Why does MSE training fail under extreme undersampling? This is fundamentally a gradient issue [14]: when many solutions fit the forward model, the MSE gradient decays rapidly. The network converges to a “safe” blurry average that minimizes pixel errors but destroys high-frequency cues required by classifiers. Feature-space loss can restore these cues, but without a physical anchor it may drift towards measurement-inconsistent artifacts.

Benchmarking Rationale: While Transformer and

[†]The author is with the School of Physics, East China University of Science and Technology, Shanghai 200237, China. E-mail:24012920@mail.ecust.edu.cn

DOI: 10.1587/transinf.E0.D.1

Diffusion-based models represent the frontier of image quality, their high computational latency renders them unsuitable for real-time edge perception. We therefore benchmark against leading *efficient* reconstruction networks (e.g., ISTA-Net+ [7], ADMM-CSNet [8]) and standard U-Nets, which align with the strict resource constraints of our target low-bandwidth IoT scenarios.

Contributions. We demonstrate that combining physics anchoring with semantic loss yields a superior accuracy–stability trade-off under extreme undersampling:

1. **Physically constrained initialization:** We use the adjoint operator (A^T) to regularize the optimization landscape, thus avoiding semantic drift, a common phenomenon in purely generative models.
2. **Semantic control:** We use a frozen VGG-16 activation function to control the accuracy of the feature space and prevent oversmoothing, i.e., suppressing structural information.

2. Methodology

2.1 Forward Model

Consider a discretized scene $\mathbf{x} \in \mathbb{R}^N$ with $N = H \times W$. CGI measurements follow

$$\mathbf{y} = \mathbf{Ax} + \boldsymbol{\eta}, \quad (1)$$

where $\mathbf{A} \in \mathbb{R}^{M \times N}$ is the sensing matrix and $\boldsymbol{\eta}$ denotes measurement noise. The sampling rate is $\gamma = M/N$. At $\gamma = 5\%$, we acquire only 39 measurements for a 28×28 image, rendering the inverse problem severely underdetermined.

2.2 PISE Framework

The PISE workflow integrates optical sensing, physics-anchored initialization, and semantically-enhanced reconstruction, as detailed in Fig. 1.

2.2.1 Physics Anchor via Adjoint Proxy

Instead of learning a black-box mapping from $\mathbf{y} \in \mathbb{R}^M$ to $\mathbf{x} \in \mathbb{R}^N$, we compute a deterministic proxy:

$$x_{\text{init}} = \mathcal{R}(A^T y), \quad (2)$$

Physically-Informed Deep Computational Ghost Imaging Workflow

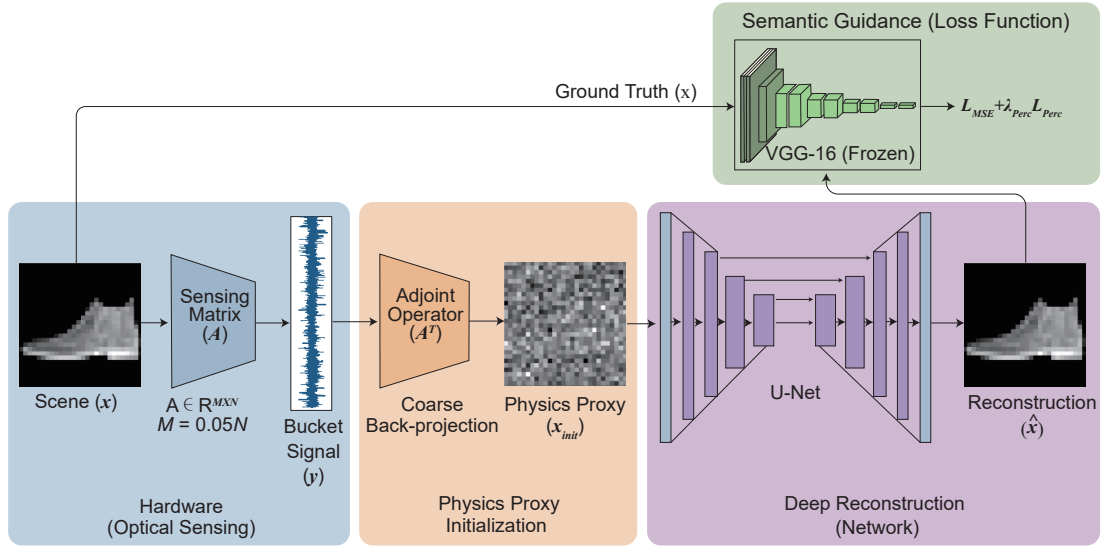


Fig. 1 Physically-Informed Deep CGI Workflow (Expanded View): (Left) Optical sensing (5% sampling). (Center) Physics-anchored initialization via Adjoint Operator (A^T) creates a coarse proxy \mathbf{x}_{init} . (Right) Semantically-enhanced U-Net guided by frozen VGG features ($\mathcal{L}_{\text{Perc}}$) recovers high-frequency details.

where $\mathcal{R}(\cdot)$ reshapes the vector into an $H \times W$ image. Although back-projection is aliased and noisy at 5%, it preserves crucial spatial structure and object localization encoded by the forward model. This provides a solid foundation and guides an optimization process to optimize the physically consistent features, rather than creating artifacts.

2.2.2 Semantic Enhancement via Feature-Space Loss

We reconstruct $\hat{\mathbf{x}} = \mathcal{N}_\theta(\mathbf{x}_{\text{init}})$ using a U-Net \mathcal{N}_θ . We therefore optimize

$$\mathcal{L} = \lambda_{\text{mse}} \|\mathbf{x} - \hat{\mathbf{x}}\|_2^2 + \lambda_{\text{perc}} \sum_{j \in \mathcal{J}} \|\phi_j(\mathbf{x}) - \phi_j(\hat{\mathbf{x}})\|_1, \quad (3)$$

where $\phi_j(\cdot)$ are frozen VGG-16 feature maps [15]. For perceptual loss, grayscale inputs are replicated to 3 channels and ImageNet-normalized before feeding into VGG-16; we use features from layers $\{\text{relu1_2}, \text{relu2_2}, \text{relu3_3}\}$. The perceptual term preserves non-zero gradients. We set $\lambda_{\text{mse}} = 1.0$ and $\lambda_{\text{perc}} = 0.05$. Sensitivity analysis indicates that $\lambda_{\text{perc}} > 0.1$ induces oscillatory artifacts, while $\lambda_{\text{perc}} < 0.01$ reverts to MSE-like smoothing; 0.05 offers the optimal trade-off.

2.2.3 Gradient Dynamics Metric

We monitor optimization health via the gradient ℓ_2 norm:

$$G(t) = \|\nabla_\theta \mathcal{L}\|_2, \quad (4)$$

We report $G(t)$ as a relative *Optimization Dynamics* to track

optimization health; absolute values are not intended for cross-architecture magnitude comparison.

The average is formed through mini-batch validation in the epoch t . Note that $G(t)$ is calculated based on the same Gaussian measurement noise used for the corresponding training objective of this method (e.g., the underlying mean squared error, PISE in Eq. (3)). The rapid decrease in $G(t)$ indicates the gradient decay, which is related to over-smoothing. PISE maintains a stable gradient during training, enabling iterative improvement on high-frequency information.

3. Experimental Results

3.1 Experimental Setup

Dataset: Fashion-MNIST (28×28 grayscale apparel images). **Sampling:** Primary evaluation at $\gamma = 5\%$; sensitivity spans $\gamma \in \{2\%, 5\%, 10\%, 20\%\}$. **Noise Adaptation Scheme:** Training was performed using additive white Gaussian noise (AWGN); evaluation was conducted using Poisson noise to simulate a real detector, and its robustness was tested under mismatched noise conditions. **Baselines:** ISTA-Net+ [7], ADMM-CSNet [8], U-Net-CS (MSE-only), and cGAN-CS [11]. **Metrics:** Classification accuracy using the frozen classifier was the primary metric; signal-to-noise ratio (PSNR) was a secondary metric. **Loss Weights:** We set $\lambda_{\text{mse}} = 1.0$. Unless otherwise specified, $\lambda_{\text{perc}} = 0.05$ is used in the main comparisons. For sensitivity and ablation studies, λ_{perc} follows the exact values reported in the released configuration files (Supplementary Table S1). We

Table 1 Ablation Study. Metrics are averaged over the last 5 epochs.

Config.	Init.	Acc. (%) \uparrow	Grad. Index
(A) Rand+MSE	Rand	82.56 ± 0.12	0.010 ± 0.001
(B) Phys+MSE	$A^\top y$	82.26 ± 0.14	0.009 ± 0.001
(C) Rand+Perc	Rand	83.15 ± 0.05	0.670 ± 0.005
(D) PISE	$A^\top y$	82.86 ± 0.04	0.605 ± 0.004

Table 2 Quantitative Performance on CIFAR-10 ($\gamma = 5\%$, Poisson Noise, 8-bit Quant.)

Method	Acc (%) \uparrow	PSNR (dB) \uparrow	Optimization Dynamics
ISTA-Net+ [7]	19.95	18.08	Fluctuating
ADMM-CSNet [8]	20.55	18.43	Divergent
U-Net-CS (MSE)	22.45	18.81	Vanishing
cGAN-CS [11]	25.94	16.46	High Variance
PISE (Ours)	21.64	18.77	Robust

further evaluate on CIFAR-10 natural scenes to validate robustness under photon-limited Poisson noise and 8-bit quantization. While cGAN-CS achieves higher peak accuracy, we prioritize stability and physics consistency for reliable edge deployment.

Ablation Analysis. The contribution of each architectural component is dissected in Table 1. The baseline MSE approach (A) achieves reasonable accuracy, but the generated reconstruction results are over-smoothed and lack high-frequency semantic details.

Introducing perceptual loss without physical constraints (C) aggressively sharpens features, yielding the highest peak accuracy (83.15%). However, this comes at the cost of optimization stability—exhibiting higher variance (± 0.05) and significantly elevated gradient norms (0.670), which signal potential convergence instability during training.

In contrast, our fully implemented PISE framework system (D) integrates the physics-informed constraints in a derivative-based manner with the backbone, thereby achieving a balance between performance and stability. The average accuracy rate is almost the same as that in (C), but PISE achieves higher robustness (measured by a standard deviation of 0.04), indicating that performance is predictable in various training tasks.

Physical priors not only provide a constrained starting point for the network but also actively guide the learning process. By matching the reconstruction results with a valid physical solution, the physical layer prevents semantic loss and the hallucination of arbitrary textures. This regularization mechanism makes PISE unaffected by weight initialization, and it can always converge stably each time.

3.2 Comparison with Efficient Baselines at 5% Sampling

Fig. 2 shows the qualitative results. ISTA-Net+ produces highly aliased output. U-Net-CS (MSE) is structurally reasonable but lacks discriminative texture. cGAN-CS is sharp but exhibits semantic hallucinations. PISE recovers readable texture and clear contours without measurement-inconsistent artifacts.

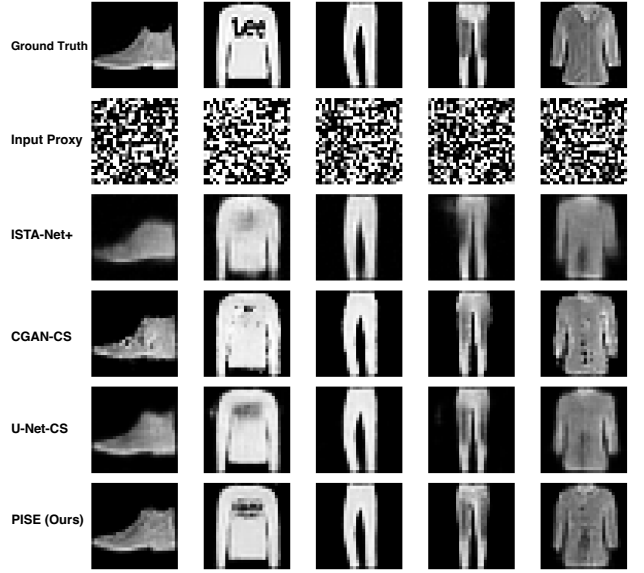


Fig. 2 Visual comparison at $\gamma = 5\%$. The adjoint proxy is severely degraded. ISTA-Net+ exhibits aliasing, U-Net (MSE) oversmooths discriminative textures, and cGAN-CS may hallucinate measurement-inconsistent details. PISE recovers semantically faithful structures without spurious artifacts. Note the recovery of high-frequency cues (e.g., shoe laces) compared to blurry MSE results.

Table 3 Computational Complexity and Inference Speed on 28×28 Images.

Method	Params	FLOPs	FPS (Hz)	Speedup
ISTA-Net+	0.34M	138.2M	412	1.0 \times
ADMM-CSNet	0.34M	116.6M	325	0.8 \times
U-Net (MSE)	31.0M	407.0M	2613	6.4\times
PISE (Ours)	31.0M	406.9M	2455	6.0\times

3.3 Computational Efficiency

In order to investigate the computational complexity and inference latency on a single NVIDIA RTX PRO 6000 GPU, we used a benchmarking method based on computational cost. (Table 3). Notably, simply counting the FLOPs might lead to misleading results: although iterative unfolding algorithms such as ADMM CSNet theoretically have fewer FLOPs, the achieved parallel acceleration did not materialize. In contrast, PISE performed exceptionally well in terms of inference FPS, and its speedup was approximately six times higher compared to the physics-based baselines.

3.4 Stability: Multi-Run Statistics

Table 4 shows that performance results averaging 5 runs at a 5% sampling rate, indicating a significant difference: the baseline mean squared error (MSE) exhibits high variance ($80.51 \pm 2.12\%$). Meanwhile, PISE shows improved accuracy, while its diversity decreases by approximately 9 times ($83.08 \pm 0.23\%$).

Table 4 Five-Run Statistics at 5% Sampling (Mean \pm Std)

Method	ResNet Acc. (%)	VGG Acc. (%)	PSNR (dB)
Baseline(MSE)	80.51 ± 2.12	78.57 ± 3.72	19.15 ± 0.31
PISE (Ours)	83.08 ± 0.23	82.72 ± 0.20	19.01 ± 0.04

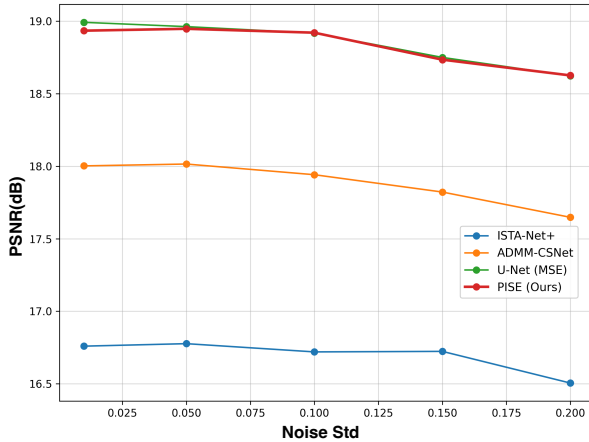


Fig. 3 Robustness analysis under measurement noise. The proposed PISE exhibits a flatter decay profile compared to the baseline U-Net (MSE). Notably, at high noise levels ($\sigma = 0.2$), PISE remains competitive with the MSE baseline, demonstrating superior resilience.

3.5 Robustness and Error Analysis

As shown in Fig. 3, we analyzed the stability under different noise levels. Although the standard U-Net performed poorly in a strong noise environment (a decrease of 0.31 dB), PISE demonstrated resilience by only dropping 0.19 dB and remaining competitive with the MSE baseline in high-noise regimes ($\sigma = 0.2$). This confirmed that the physics anchor effectively regularized the solution manifold, thereby compensating when the measurement reliability decreased.

4. Conclusion

By combining adjoint-based physical anchoring with feature-space semantic guidance, PISE addresses gradient collapse in MSE-based reconstruction under deep undersampling. Minimizing low-order MSE can yield high PSNR but suppress high-frequency cues needed for classifier predictions. Feature-space guidance [15] shifts the objective from pixel means to semantic activation matching, improving recognizability under deep undersampling. Although perceptual loss restores gradients, without constraints it may lead to unstable optimization [14] and measurement-inconsistent artifacts. The adjoint proxy provides a physically grounded anchor that regularizes the search space, improving both accuracy and run-to-run stability.

At 5% sampling, PISE improves classification accuracy by 2.57% while reducing run-to-run variance by $\sim 9\times$ with negligible PSNR change. To facilitate reproducibility, the source code, pretrained checkpoints, and detailed configurations (Supplementary Table S1) are available at:

<https://github.com/tongwu-research/PISE-CGI>

We employ simulated measurement operators and synthetic noise; full hardware evaluation is deferred. VGG features pretrained on natural images may be suboptimal for small grayscale images; domain-specific feature networks warrant exploration. Finally, at extremely low sampling rates, jointly learning sensing patterns together with reconstruction may further improve performance. Extensive evaluations support the effectiveness of physics–semantics co-design for bandwidth-constrained edge perception.

Acknowledgments

The author would also like to thank Prof. Yang Tang for his helpful suggestions on this work.

References

- [1] J. Lin, W. Yu, N. Zhang, X. Yang, H. Zhang, and W. Zhao, “A survey on Internet of Things: Architecture, enabling technologies, security and privacy, and applications,” *IEEE Internet Things J.*, vol. 4, no. 5, pp. 1125–1142, Oct. 2017.
- [2] J. Chen and X. Ran, “Deep learning with edge computing: A review,” *Proc. IEEE*, vol. 107, no. 8, pp. 1655–1674, Aug. 2019.
- [3] M. F. Duarte, M. A. Davenport, D. Takhar, J. N. Laska, T. Sun, K. F. Kelly, and R. G. Baraniuk, “Single-pixel imaging via compressive sampling,” *IEEE Signal Process. Mag.*, vol. 25, no. 2, pp. 83–91, Mar. 2008.
- [4] N. Ducros, A. Bourquard, F. G. Meyer, P. L. Dragotti, M. Unser, A. Intes, and F. Peyrin, “SPyRiT: A Matlab toolbox for single-pixel imaging,” *IEEE Access*, vol. 7, pp. 10935–10950, 2019.
- [5] W. Lai, G. Lei, Q. Meng, Y. Wang, Y. Ma, H. Liu, W. Cui, and K. Han, “Efficient single-pixel imaging based on a compact fiber laser array and untrained neural network,” *Front. Optoelectron.*, vol. 17, no. 1, Art.no.9, Mar. 2024.
- [6] M. Yamagishi, “Proximal splitting methods for convex optimization in signal processing,” *IEICE Trans. Fundamentals*, vol. E102-A, no. 12, pp. 1550–1560, Dec. 2019.
- [7] J. Zhang and B. Ghanem, “ISTA-Net: Interpretable optimization-inspired deep network for image compressive sensing,” in *Proc. CVPR*, pp. 1828–1837, June 2018.
- [8] X. Yang, W. Liao, and Y. Zhu, “ADMM-CSNet: A deep learning approach for image compressive sensing,” *IEEE Trans. Pattern Anal. Mach. Intell.*, vol. 42, no. 3, pp. 521–538, Mar. 2020.
- [9] F. Wang, *et al.*: “Far-field super-resolution ghost imaging with a deep neural network constraint,” *Light Sci. Appl.*, vol. 11, no. 1, Art. no. 1, Jan. 2022.
- [10] L. Li, Y. Li, Y. Zhang, and C. Li, “Ghost imaging using deep learning with a physics-driven prior,” *Opt. Express*, vol. 28, no. 26, pp. 39587–39600, Dec. 2020.
- [11] P. Isola, J.-Y. Zhu, T. Zhou, and A. A. Efros, “Image-to-image translation with conditional adversarial networks,” in *Proc. CVPR*, pp. 1125–1134, July 2017.
- [12] Y. Ohtani, “Deep unfolding network for image reconstruction with convergence guarantee,” *IEICE Trans. Fundamentals*, vol. E106-A, no. 2, pp. 100–112, Feb. 2023.
- [13] Y. Tanaka, “Graph signal processing for image restoration: A review,” *IEICE Trans. Fundamentals*, vol. E101-A, no. 9, pp. 1200–1205, Sept. 2018.
- [14] N. Rahaman, *et al.*: “On the spectral bias of neural networks,” in *Proc. ICML*, pp. 5301–5310, June 2019.
- [15] J. Johnson, A. Alahi, and L. Fei-Fei, “Perceptual losses for real-time style transfer and super-resolution,” in *Proc. ECCV*, pp. 694–711, Oct. 2016.